Projection-Method Solution of the Lid-Driven Cavity Problem

Rithwik Shankar Raj

1 Introduction

The lid-driven cavity problem is a standard benchmark in incompressible computational fluid dynamics because it combines a simple geometry with nontrivial flow physics. A square cavity is enclosed by stationary walls on three sides, while the top wall moves with a constant tangential velocity. This motion induces a recirculating flow field inside the cavity, generating a primary vortex and, with increasing Reynolds number, stronger shear layers and corner vortices.

In the present work, the flow is solved using the projection method on a staggered grid. In this approach, the incompressible Navier–Stokes equations are advanced in two stages. First, an intermediate velocity field is computed from the momentum equations without the pressure gradient term. Second, a pressure Poisson equation is solved and the velocity field is corrected so that the final velocity satisfies incompressibility.

2 Problem Definition

A square cavity of side length $L = H = 1$ is considered. The top lid moves with a constant velocity

$$U_{\text{lid}} = 1,$$

while the left, right, and bottom walls are stationary and satisfy no-slip boundary conditions. Two cases are studied:

$$Re = 100, \qquad Re = 400.$$

The Reynolds number is defined as

$$Re = \frac{\rho U_{\text{lid}} L}{\mu}.$$

With the nondimensional choices

$$L = 1, \qquad H = 1, \qquad \rho = 1, \qquad U_{\text{lid}} = 1,$$

the kinematic viscosity becomes

$$\nu = \frac{1}{Re}.$$

Table 1: Simulation parameters for the lid-driven cavity problem.

Quantity	Value
Cavity length, L	1
Cavity height, H	1
Lid velocity, U_{lid}	1
Density, ρ	1
Reynolds numbers considered	100, 400
Kinematic viscosity, ν	$1/Re$
Convergence tolerance	10^{-7}
Grid sizes for convergence study	$N = 22,\ 44,\ 88$
Finest reference grid	$N = 102$

3 Projection Method Formulation

3.1 Algorithm overview

The projection method proceeds through the following steps:

1. Solve the momentum equations without the pressure terms to obtain an intermediate velocity field $\boldsymbol{u}^*$ that is generally not divergence free.
2. Solve the pressure Poisson equation by enforcing the divergence-free constraint.
3. Project the intermediate velocity onto a divergence-free space using the computed pressure.

Pressure therefore acts as a Lagrange multiplier that enforces continuity.

3.2 Domain and staggered-grid arrangement

The physical domain is a square cavity with a moving lid on the upper boundary. A staggered-grid layout is used in the numerical implementation: pressure is stored at cell centers, the horizontal velocity u is stored at vertical cell faces, and the vertical velocity v is stored at horizontal cell faces. This arrangement suppresses pressure–velocity decoupling and is standard for incompressible flow calculations.

3.3 Governing equations

The incompressible Navier–Stokes equations in nondimensional form are

$$\nabla \cdot \boldsymbol{u} = 0, \tag{1}$$

$$\frac{\partial \boldsymbol{u}}{\partial t} + (\boldsymbol{u} \cdot \nabla)\boldsymbol{u} = -\nabla p + \frac{1}{Re}\nabla^2 \boldsymbol{u}. \tag{2}$$

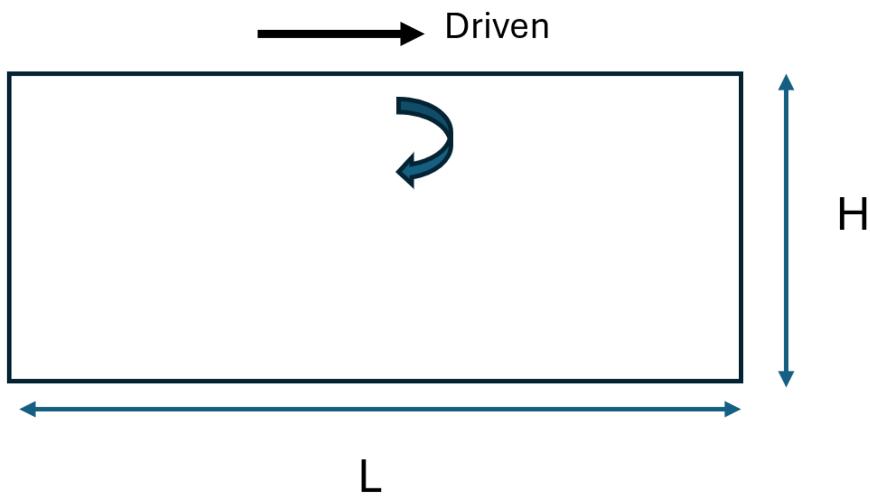

Figure 1: Schematic of the lid-driven cavity domain.

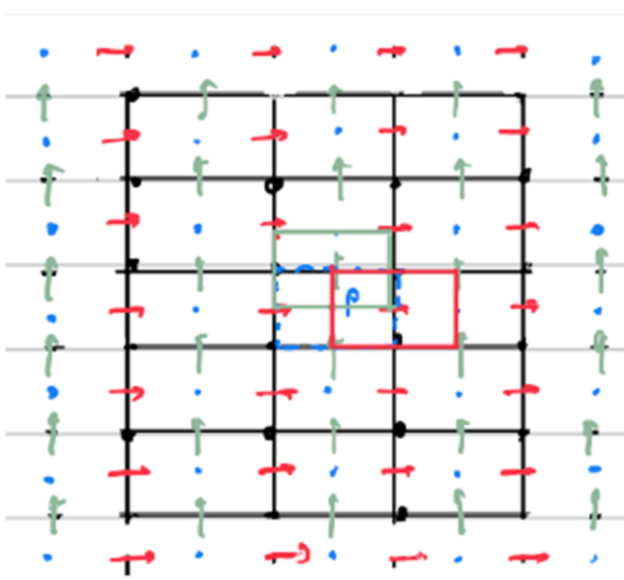

Figure 2: Staggered-grid arrangement showing the locations of pressure and velocity variables.

Writing the momentum equations component-wise gives

$$\frac{\partial u}{\partial t} + \frac{\partial (u^2)}{\partial x} + \frac{\partial (uv)}{\partial y} = -\frac{\partial p}{\partial x} + \frac{1}{Re}\left(\frac{\partial^2 u}{\partial x^2} + \frac{\partial^2 u}{\partial y^2}\right), \tag{3}$$

$$\frac{\partial v}{\partial t} + \frac{\partial (uv)}{\partial x} + \frac{\partial (v^2)}{\partial y} = -\frac{\partial p}{\partial y} + \frac{1}{Re}\left(\frac{\partial^2 v}{\partial x^2} + \frac{\partial^2 v}{\partial y^2}\right). \tag{4}$$

3.4 Step 1: intermediate velocity field

The first step in the projection method is to solve the momentum equations while neglecting the pressure gradient. This produces an intermediate velocity field $\boldsymbol{u}^*$:

$$\frac{\partial \boldsymbol{u}^*}{\partial t} + (\boldsymbol{u} \cdot \nabla)\boldsymbol{u} = \nu \nabla^2 \boldsymbol{u}, \tag{5}$$

or equivalently,

$$\frac{\boldsymbol{u}^* - \boldsymbol{u}^n}{\Delta t} + (\boldsymbol{u}^n \cdot \nabla)\boldsymbol{u}^n = \nu \nabla^2 \boldsymbol{u}^n. \tag{6}$$

Here, $\boldsymbol{u}^n$ is the velocity at time level n, and $\boldsymbol{u}^*$ is the intermediate velocity.

3.5 Discrete x-momentum equation

For the horizontal velocity component, the derivation leads to

$$\frac{u^*_{i,j} - u^n_{i,j}}{\Delta t} = -\frac{u_e^2 - u_w^2}{\Delta x} - \frac{u_n v_n - u_s v_s}{\Delta y} + \frac{1}{Re}\left[\frac{u^n_{i,j+1} - 2u^n_{i,j} + u^n_{i,j-1}}{\Delta x^2} + \frac{u^n_{i+1,j} - 2u^n_{i,j} + u^n_{i-1,j}}{\Delta y^2}\right]. \tag{7}$$

The face-interpolated quantities are

$$u_e = \frac{u_{i,j} + u_{i,j+1}}{2}, \qquad u_w = \frac{u_{i,j} + u_{i,j-1}}{2}, \tag{8}$$

$$u_s = \frac{u_{i,j} + u_{i-1,j}}{2}, \qquad u_n = \frac{u_{i,j} + u_{i+1,j}}{2}, \tag{9}$$

$$v_n = \frac{v_{i,j} + v_{i,j+1}}{2}, \qquad v_s = \frac{v_{i-1,j} + v_{i-1,j+1}}{2}. \tag{10}$$

For compactness, the update may be written as

$$u^*_{i,j} = u^n_{i,j} + \Delta t \left[\mathrm{adv}_u + \mathrm{diff}_u\right], \tag{11}$$

where the advection and diffusion terms are those appearing in Eq. (7).

3.6 Discrete y-momentum equation

For the vertical velocity component, the discrete intermediate update is

$$\frac{v^*_{i,j} - v^n_{i,j}}{\Delta t} = -\frac{v_e u_e - v_w u_w}{\Delta x} - \frac{v_n^2 - v_s^2}{\Delta y} + \frac{1}{Re}\left[\frac{v^n_{i,j+1} - 2v^n_{i,j} + v^n_{i,j-1}}{\Delta x^2} + \frac{v^n_{i+1,j} - 2v^n_{i,j} + v^n_{i-1,j}}{\Delta y^2}\right]. \tag{12}$$

The interpolated quantities are

$$v_e = \frac{v_{i,j} + v_{i,j+1}}{2}, \qquad v_w = \frac{v_{i,j} + v_{i,j-1}}{2}, \tag{13}$$

$$v_s = \frac{v_{i-1,j} + v_{i,j}}{2}, \qquad v_n = \frac{v_{i+1,j} + v_{i,j}}{2}, \tag{14}$$

$$u_e = \frac{u_{i+1,j} + u_{i,j}}{2}, \qquad u_w = \frac{u_{i+1,j-1} + u_{i,j-1}}{2}. \tag{15}$$

The compact form is

$$v^*_{i,j} = v^n_{i,j} + \Delta t \left[\text{adv}_v + \text{diff}_v\right]. \tag{16}$$

3.7 Step 2: pressure Poisson equation

The correction step can be written as

$$\frac{\boldsymbol{u}^{n+1} - \boldsymbol{u}^*}{\Delta t} = -\nabla p. \tag{17}$$

Taking the divergence of both sides gives

$$\frac{\nabla \cdot \boldsymbol{u}^{n+1} - \nabla \cdot \boldsymbol{u}^*}{\Delta t} = -\nabla^2 p. \tag{18}$$

Since the corrected velocity field must satisfy incompressibility,

$$\nabla \cdot \boldsymbol{u}^{n+1} = 0,$$

and the pressure Poisson equation becomes

$$\nabla^2 p = \frac{1}{\Delta t} \nabla \cdot \boldsymbol{u}^*. \tag{19}$$

On the staggered grid, the corresponding discrete form is

$$\frac{p_{i+1,j} - 2p_{i,j} + p_{i-1,j}}{\Delta x^2} + \frac{p_{i,j+1} - 2p_{i,j} + p_{i,j-1}}{\Delta y^2} = \frac{1}{\Delta t}\left[\frac{u^*_{i,j+1} - u^*_{i,j}}{\Delta x} + \frac{v^*_{i+1,j} - v^*_{i,j}}{\Delta y}\right]. \tag{20}$$

This equation is solved using a Gauss–Seidel SOR procedure.

3.8 Step 3: velocity projection

Once the pressure is known, the intermediate velocity field is corrected:

$$\boldsymbol{u}^{n+1} = \boldsymbol{u}^* - \Delta t \nabla p. \tag{21}$$

On the staggered grid, the component-wise updates are

$$u_{i,j}^{n+1} = u_{i,j}^{*} - \Delta t \, \frac{p_{i,j+1} - p_{i,j}}{\Delta x}, \tag{22}$$

$$v_{i,j}^{n+1} = v_{i,j}^{*} - \Delta t \, \frac{p_{i+1,j} - p_{i,j}}{\Delta y}. \tag{23}$$

3.9 Boundary conditions

The physical boundary conditions for the lid-driven cavity are

$$u(x,1) = U_{\text{lid}} = 1, \qquad v(x,1) = 0, \tag{24}$$

$$u(x,0) = 0, \qquad v(x,0) = 0, \tag{25}$$

$$u(0,y) = 0, \qquad v(0,y) = 0, \tag{26}$$

$$u(1,y) = 0, \qquad v(1,y) = 0. \tag{27}$$

The pressure satisfies homogeneous Neumann conditions at the walls,

$$\frac{\partial p}{\partial n} = 0, \tag{28}$$

which, in ghost-cell form, may be written schematically as

$$p_{\text{ghost}} = p_{\text{adjacent}}. \tag{29}$$

A second-order ghost-cell treatment is

Top wall: $$p_{i,N+1} = p_{i,N}, \qquad u_{i,N+1} = 2U_{\text{lid}} - u_{i,N}, \qquad v_{i,N+1} = -v_{i,N}, \tag{30}$$

Bottom wall: $$p_{i,0} = p_{i,1}, \qquad u_{i,0} = -u_{i,1}, \qquad v_{i,0} = -v_{i,1}, \tag{31}$$

Side walls: $$p_{0,j} = p_{1,j}, \quad p_{N+1,j} = p_{N,j}, \qquad u_{0,j} = -u_{1,j}, \quad u_{N+1,j} = -u_{N,j}, \qquad v_{0,j} = -v_{1,j}, \quad v_{N+1,j} = - \tag{32}$$

4 Numerical Procedure

The solution procedure for each timestep is summarized below:

1. Initialize u, v, and p on the staggered grid.
2. Apply the lid and wall boundary conditions.
3. Compute the intermediate velocity field (u^*, v^*) from the momentum equations.
4. Solve the pressure Poisson equation using the divergence of the intermediate field as the source term.

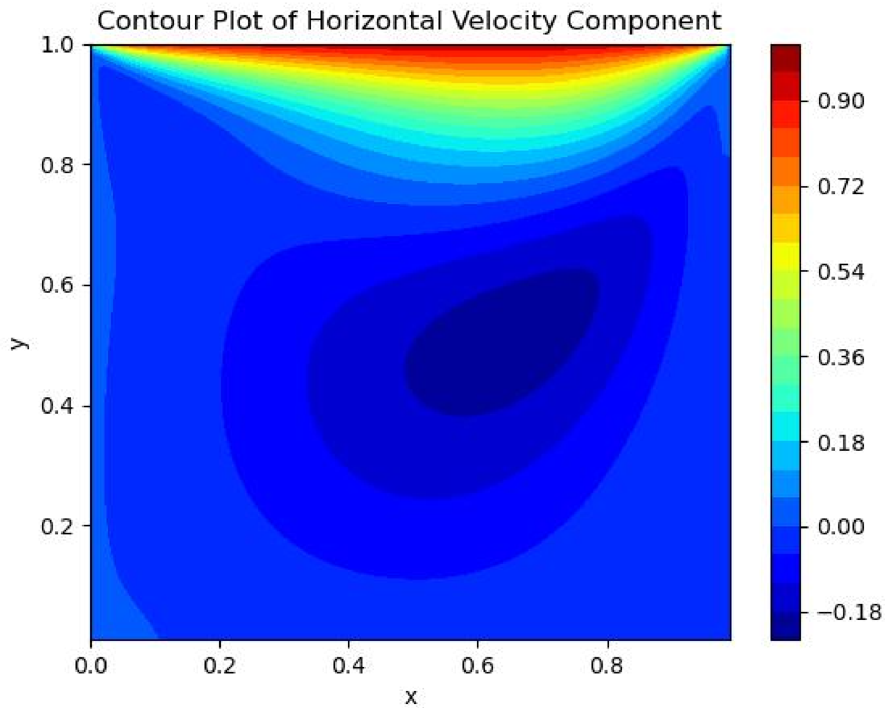

Figure 3: Plot of the horizontal velocity (u) for $Re = 100$.

5. Correct the intermediate velocity to obtain (u^{n+1}, v^{n+1}).
6. Evaluate the convergence metric based on the L_2 norm of the velocity change:

$$\mathcal{R}^{(n)} = \left[\sum_{i,j} \left(u_{i,j}^{n+1} - u_{i,j}^{n} \right)^2 + \sum_{i,j} \left(v_{i,j}^{n+1} - v_{i,j}^{n} \right)^2 \right]^{1/2}. \tag{33}$$

7. Repeat until the prescribed tolerance $\mathcal{R}^{(n)} < 10^{-7}$ is reached.

After convergence, the staggered velocity field is interpolated to a collocated representation for post-processing. Surface plots, contours, centerline velocity profiles, and streamline plots are then generated.

5 Results and Discussion

5.1 Case I: Reynolds number $Re = 100$

For $Re = 100$, the projection method produces a laminar cavity flow dominated by viscous effects. The horizontal velocity is largest near the moving lid and decreases toward the bottom of the cavity. The vertical velocity field reflects the recirculating motion induced by the lid, with stronger upward and downward motion appearing in the interior and near the walls.

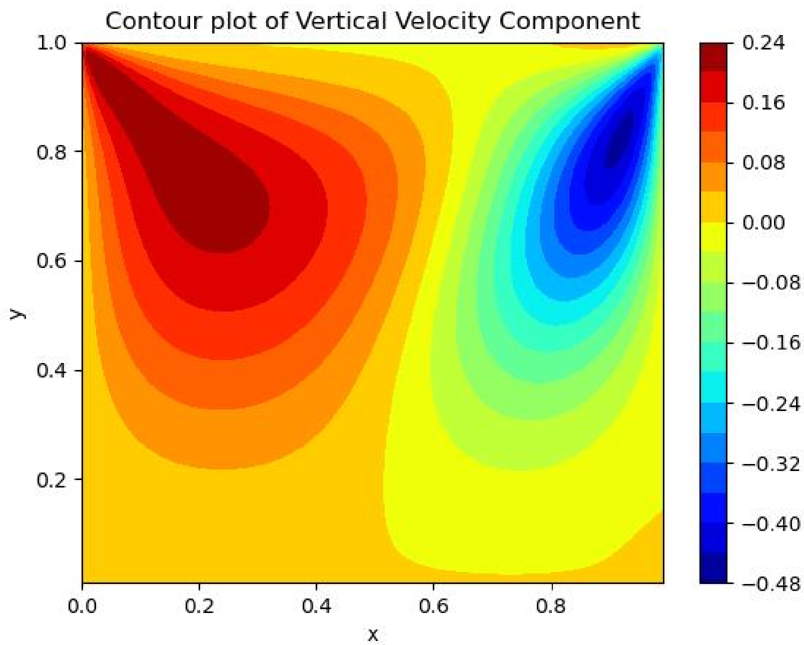

Figure 4: Plot of vertical component of velocity (v) for $Re = 100$.

A primary vortex forms near the center of the cavity. At this Reynolds number the contours remain smooth and relatively symmetric, indicating gradual variation of velocity in the domain. Boundary layers are visible near the moving lid and the side walls, and the redirection of the flow near the corners is clearly reflected in the vertical-velocity distribution.

The solution is advanced until the L_2 norm of the velocity change falls below the specified tolerance. For this case, the residual decreases steadily and reaches the stopping criterion after approximately 1.2×10^4 iterations.

To assess solution accuracy, the centerline horizontal velocity $u(y)$ and the centerline vertical velocity $v(x)$ are compared against the benchmark data of Ghia et al. The numerical results follow the expected benchmark trends closely.

The agreement with the benchmark data is close for both centerline profiles. The reference data from Ghia et al. were first tabulated and then interpolated prior to plotting.

The streamline plot of the net velocity magnitude and the contour plot of the horizontal velocity further confirm the dominant central recirculation. The corners show the early development of recirculation zones, but these remain comparatively weak at $Re = 100$.

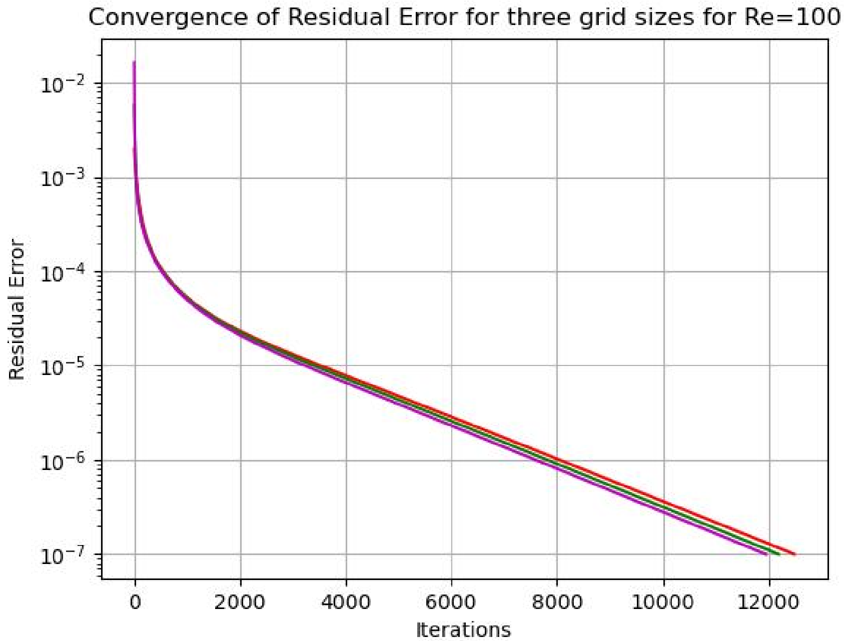

Figure 5: Plot of residual error with iterations for $Re = 100$.

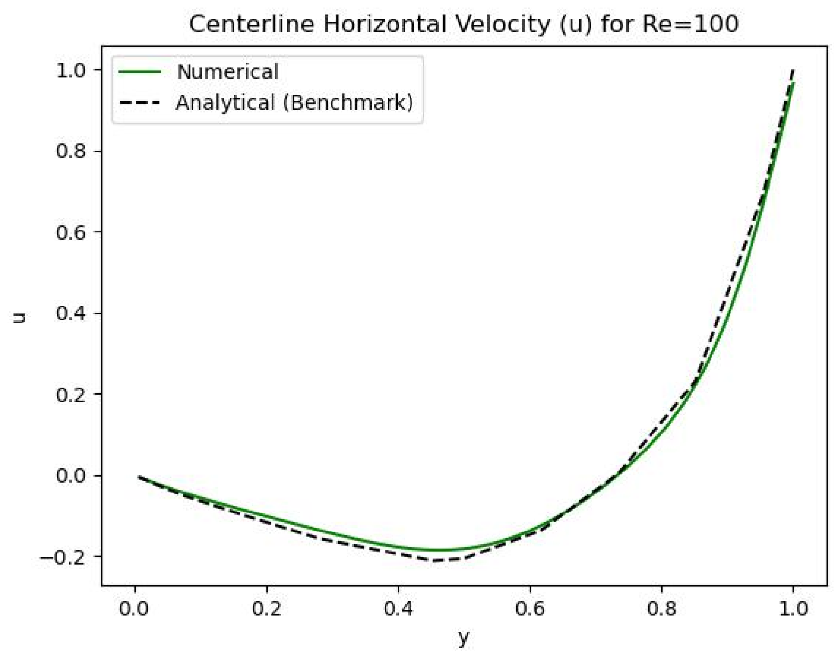

Figure 6: Centerline horizontal velocity (u) for $Re = 100$.

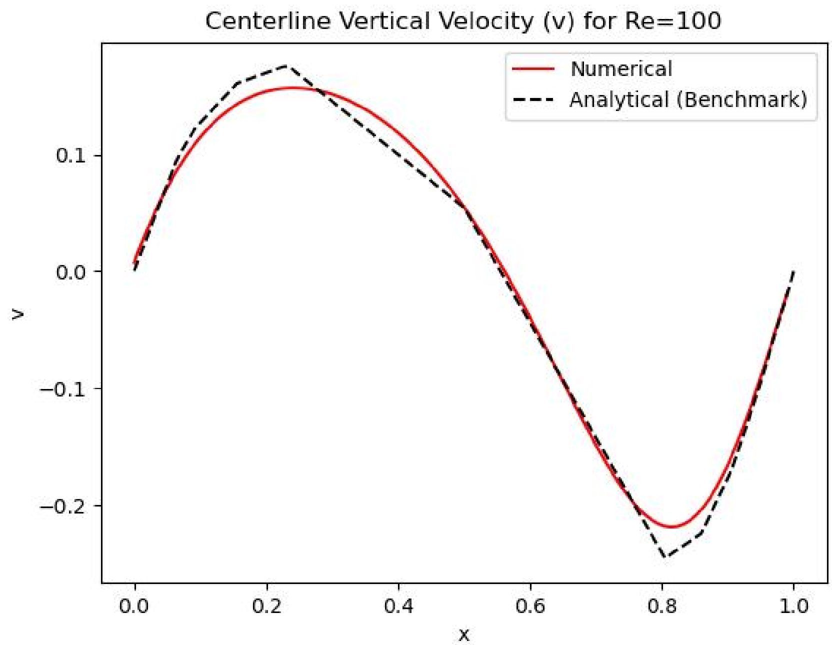

Figure 7: Centerline vertical velocity (v) for $Re = 100$.

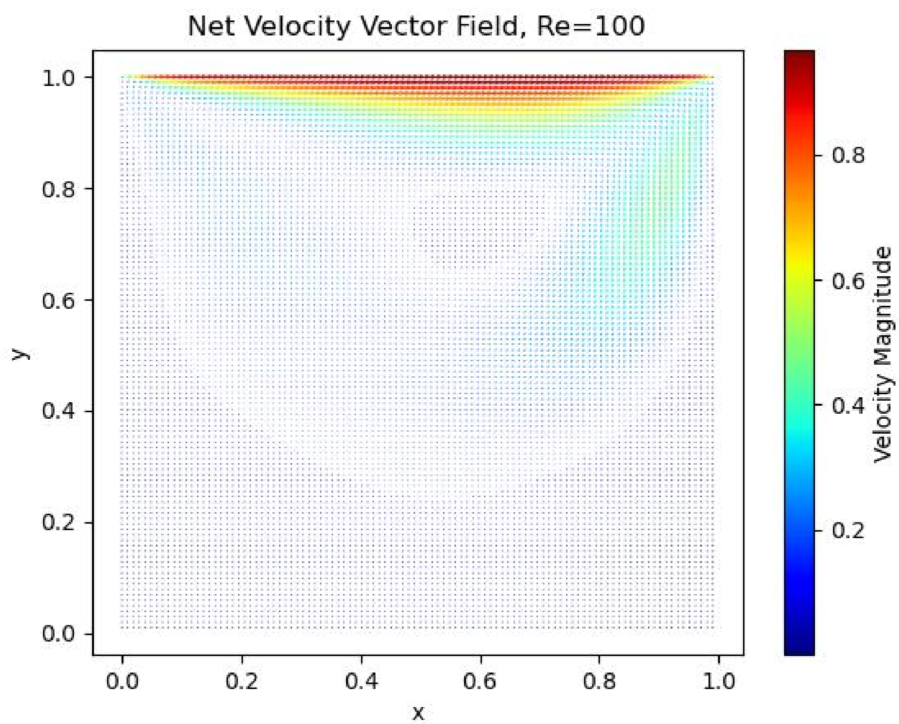

Figure 8: Streamline plot of net velocity vector for $Re = 100$.

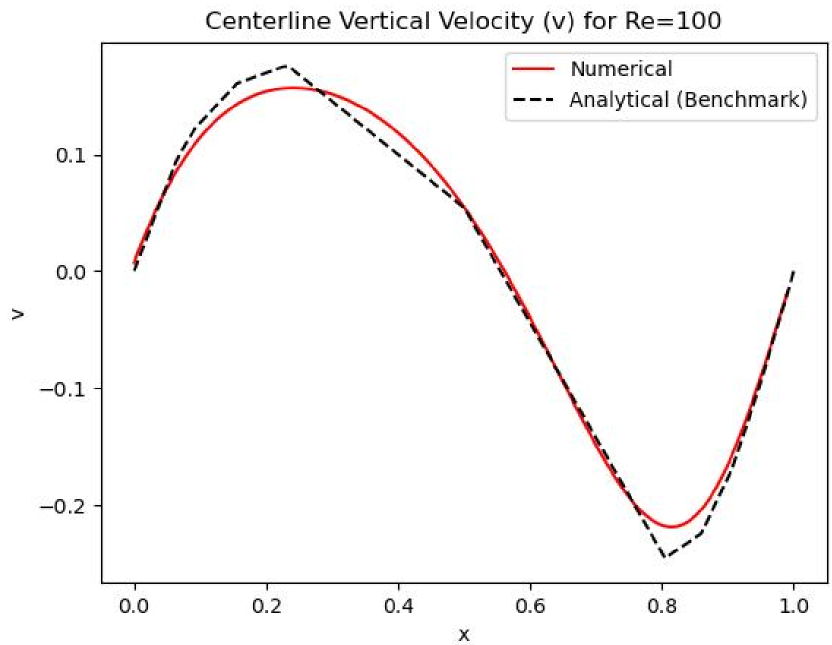

Figure 9: Centerline vertical velocity (v) for $Re = 100$.

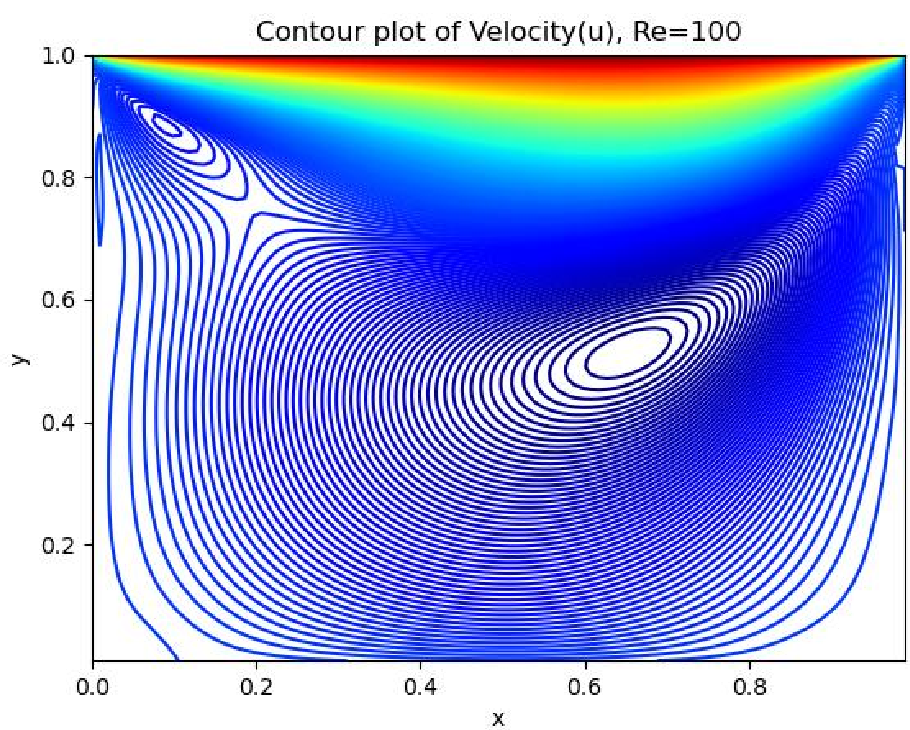

Figure 10: Contour plot of horizontal velocity (u) for $Re = 100$.

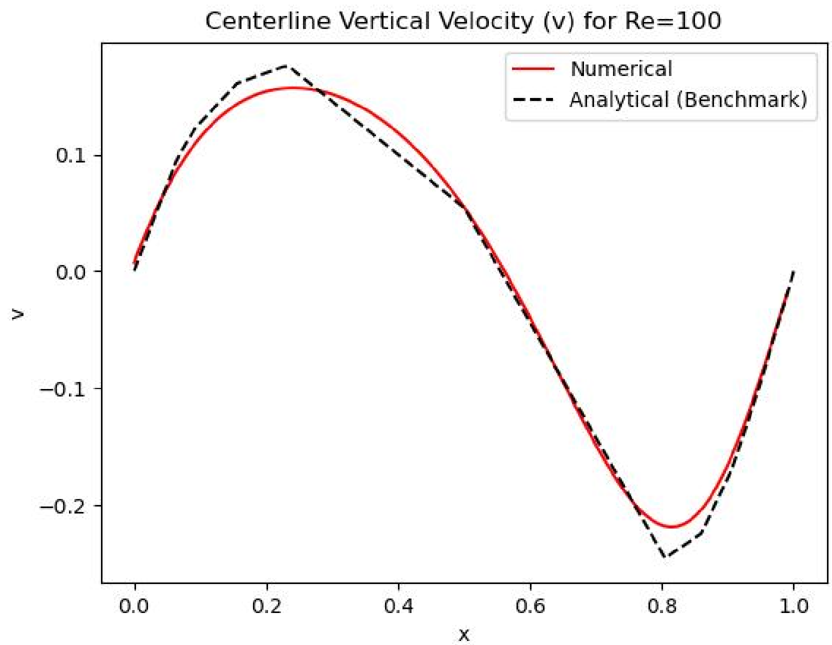

Figure 11: Centerline vertical velocity (v) for $Re = 100$.

5.2 Case II: Reynolds number $Re = 400$

At $Re = 400$, inertial effects become more significant and the velocity field becomes more asymmetric. The primary vortex remains dominant but is more distorted than in the lower-Reynolds-number case, and sharper gradients appear near the lid and in the corner regions.

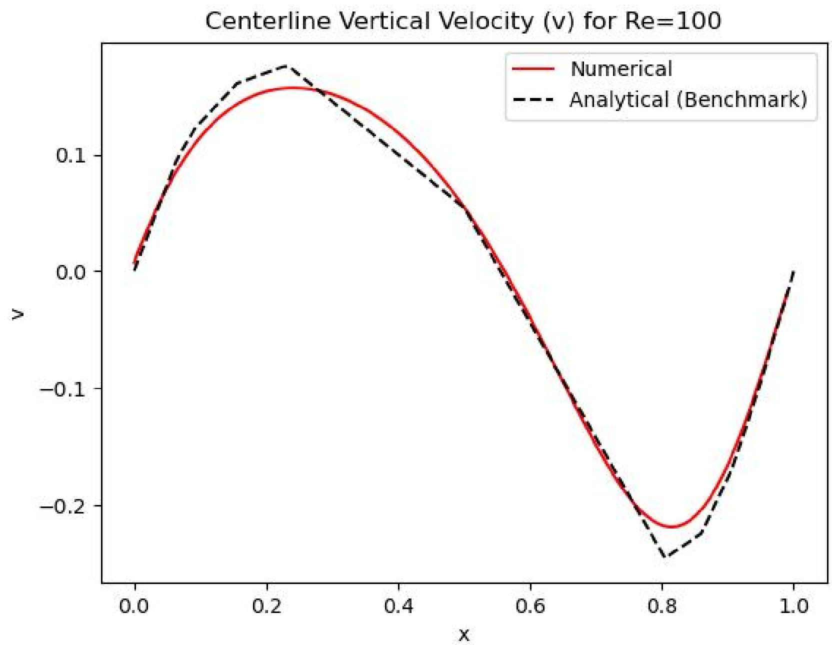

Figure 13: Centerline vertical velocity (v) for $Re = 100$.

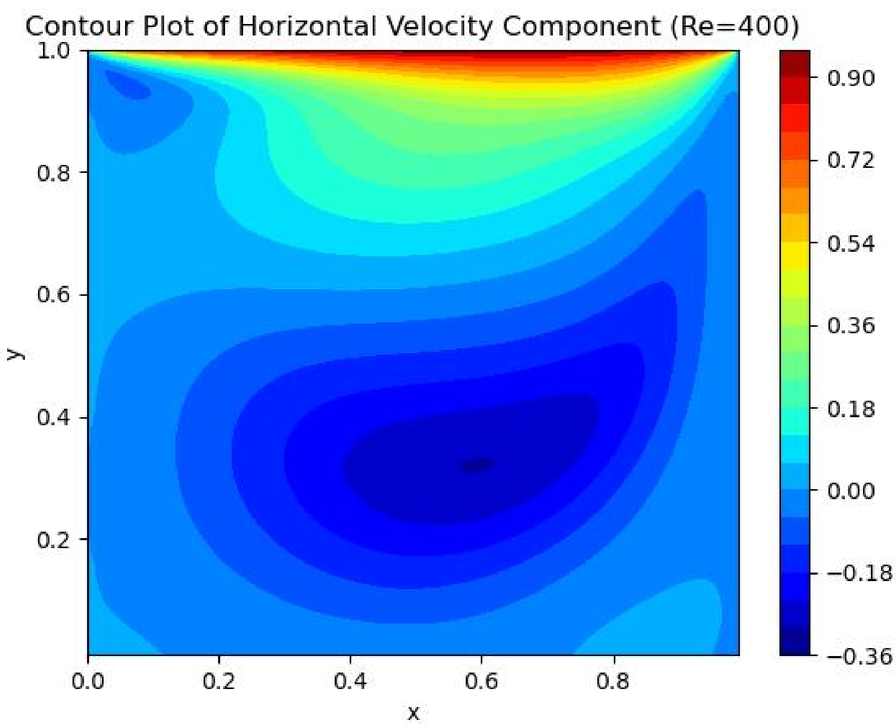

Figure 12: Plot of the horizontal velocity (u) for $Re = 400$.

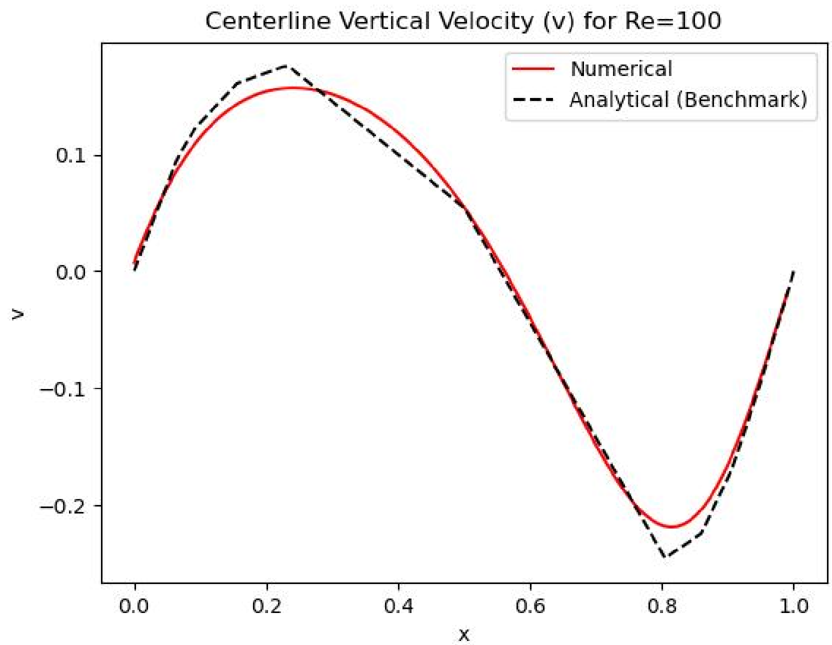

Figure 15: Centerline vertical velocity (v) for $Re = 100$.

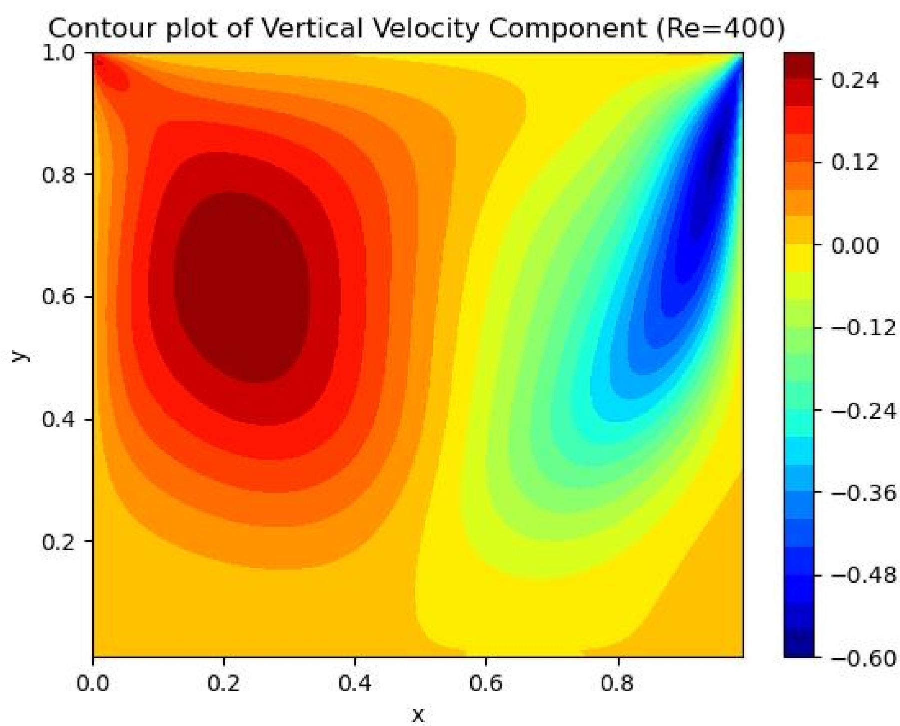

Figure 14: Plot of vertical component of velocity (v) for $Re = 400$.

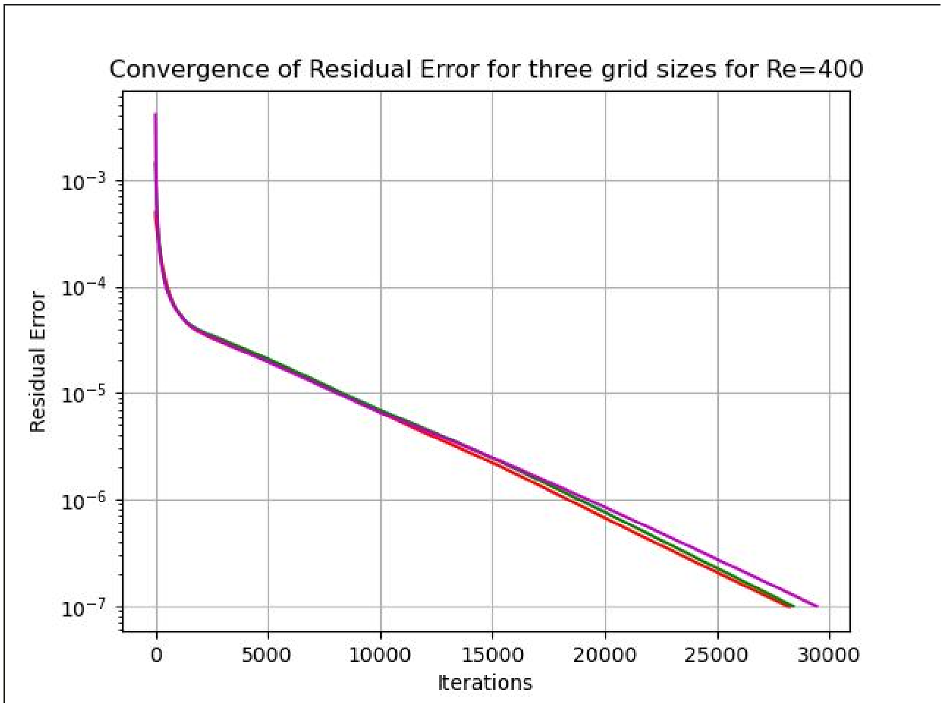

Figure 16: Plot of residual error with iterations for $Re = 400$.

The horizontal-velocity contours highlight thinner boundary layers and stronger gradients, while the vertical-velocity field shows more pronounced recirculating motion and stronger shear near the corners. These changes are consistent with the increase in Reynolds number and the corresponding reduction in viscous dominance.

The residual still decays overall, but the higher-Reynolds-number case shows stronger fluctuations in local velocities and residual history. Approximately 3.0×10^4 iterations are required to reach the steady-state tolerance.

As with the $Re = 100$ case, the centerline velocity profiles are compared against the benchmark solution. The numerical profiles again show close agreement and capture the expected changes in the velocity extrema and vortex structure.

The streamline and contour plots reveal stronger secondary recirculation near the corners than in the $Re = 100$ case. The contour plot with a finer level set also shows more clearly the emergence of corner-vortex structures.

6 Grid-Convergence Assessment

To validate the spatial behavior of the numerical scheme, the centerline velocity profiles were computed on three grid resolutions,

$$N = 22, \qquad 44, \qquad 88,$$

with the grid spacing halved at each refinement step. The centerline horizontal and vertical velocities were compared for both Reynolds numbers.

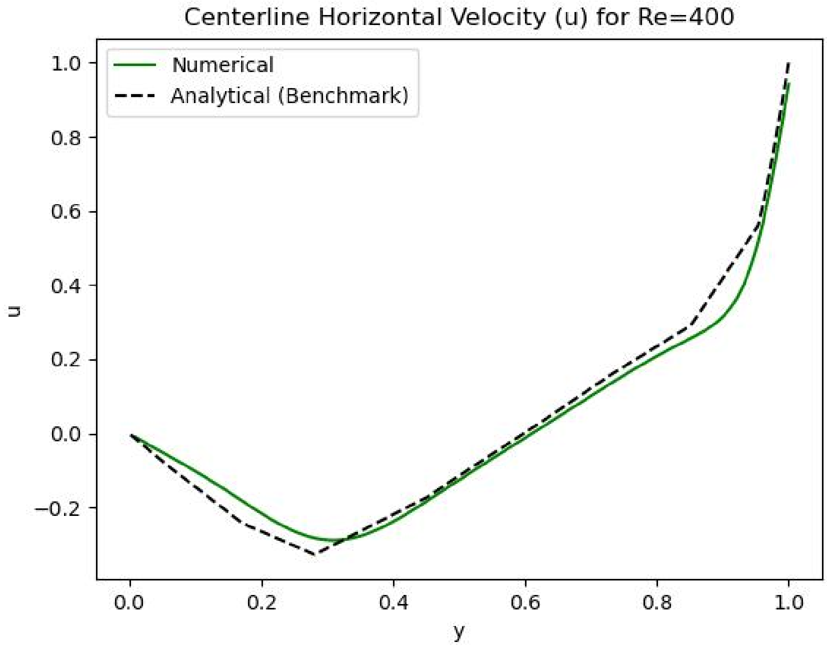

Figure 17: Centerline horizontal velocity (u) for $Re = 400$.

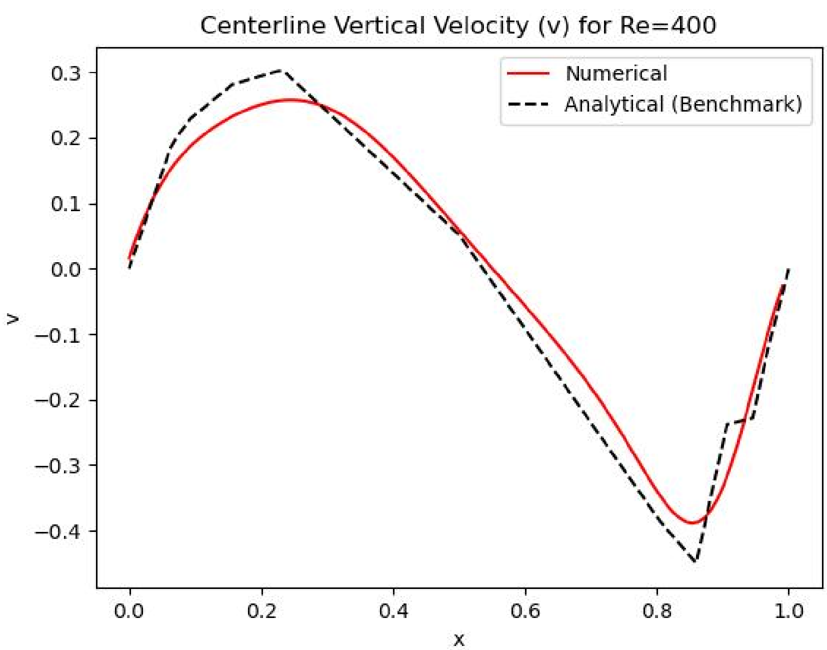

Figure 18: Centerline vertical velocity (v) for $Re = 400$.

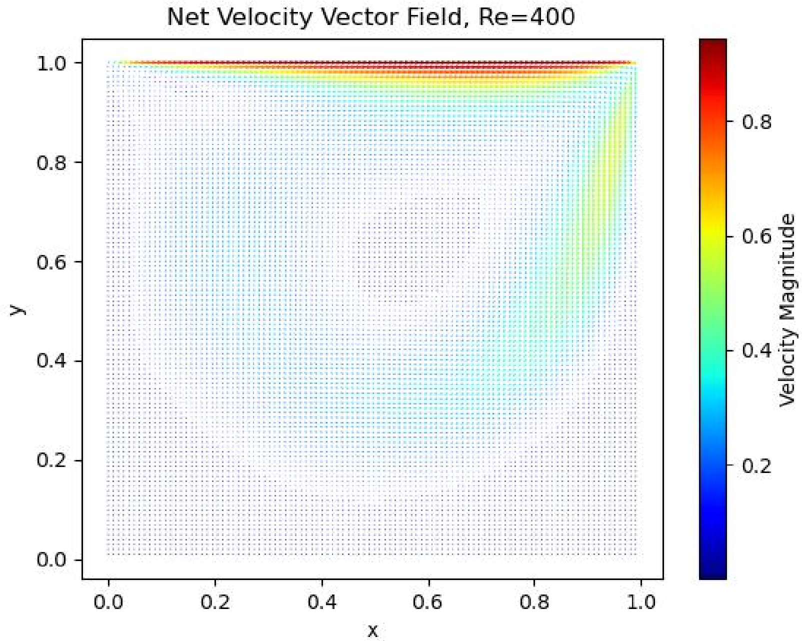

Figure 19: Streamline plot of net velocity vector for $Re = 400$.

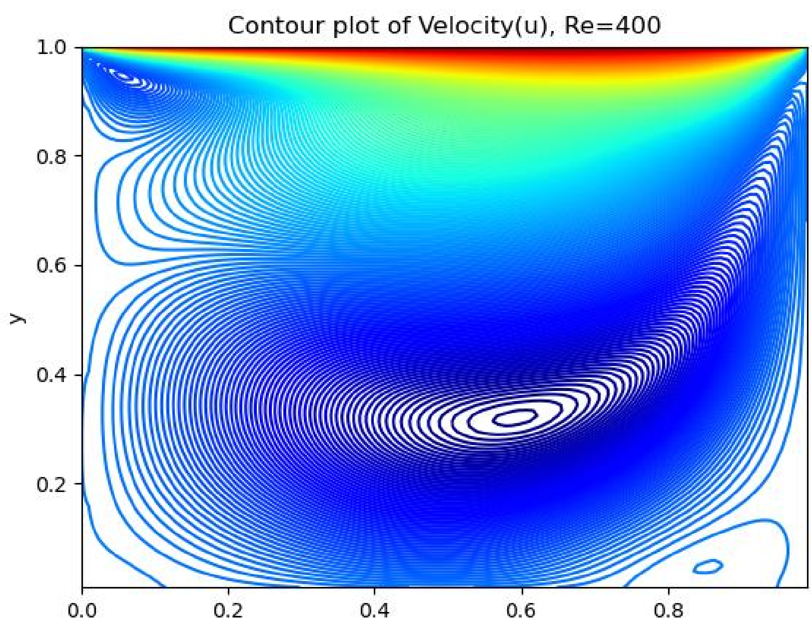

Figure 20: Contour plot of horizontal velocity (u) for $Re = 400$.

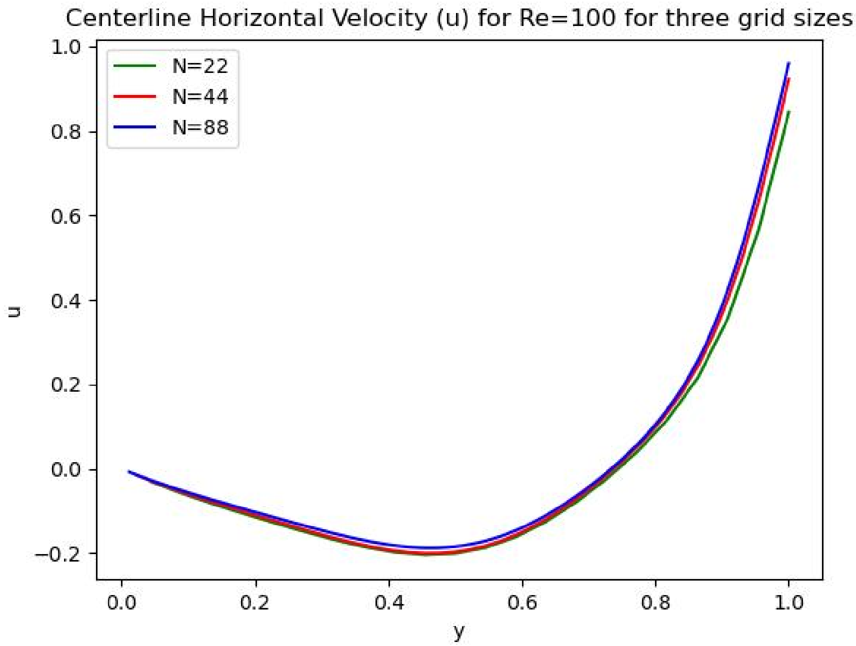

Figure 21: Centerline horizontal velocity for three grid sizes ($N = 22, 44, 88$) for $Re = 100$.

For $Re = 100$, the centerline profiles move progressively closer to the benchmark data as the mesh is refined. This improvement indicates that the numerical solution captures boundary-layer behavior and vortex structure more accurately on finer grids.

As the mesh is refined from $N = 22$ to $N = 88$, the profiles exhibit smoother transitions and better agreement with the literature values.

For $Re = 400$, the same refinement trend is observed. The horizontal centerline velocity aligns more closely with the benchmark in the primary-vortex region, and the vertical centerline velocity more accurately captures the stronger flow reversal and overall cavity symmetry.

7 Spatial-Convergence Rate

A spatial-convergence study was also performed by comparing residual histories and error norms across the three grid sizes. For each grid, the residual error was monitored as the solution advanced toward steady state.

Using progressively finer grids made it possible to observe the reduction of error with increasing spatial resolution. As expected, finer grids required more iterations to converge because of the larger number of computational points, but they also produced more accurate velocity fields.

Taking the finest grid, $N = 102$, as the reference solution, the L_2 norm of the error was evaluated for the coarser grids. The resulting error curves show a monotonic decrease as the grid is refined, indicating that the discretization is converging toward the fine-grid solution.

The observed trend is consistent with second-order spatial accuracy for the discretization used in

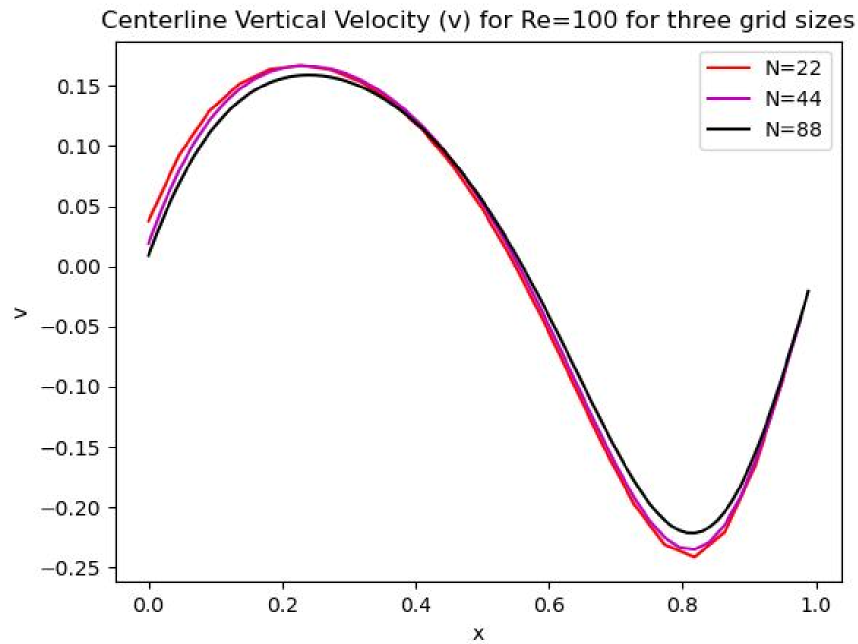

Figure 22: Centerline vertical velocity for three grid sizes ($N = 22, 44, 88$) for $Re = 100$.

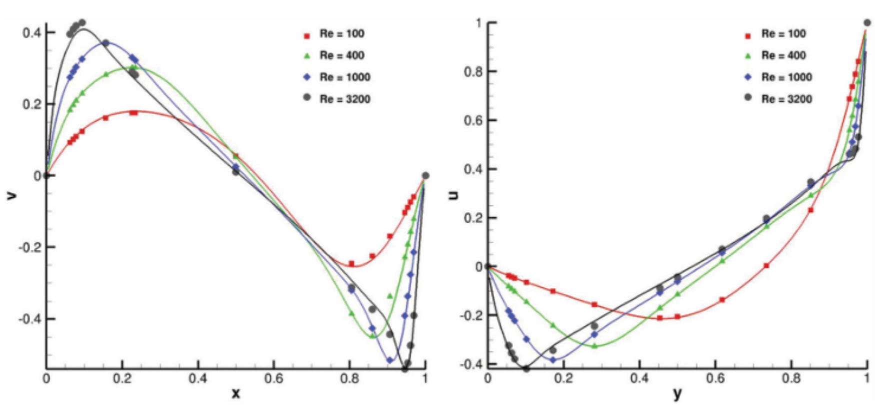

Figure 23: Centerline velocities for the lid-driven cavity: (a) vertical velocity variation and (b) horizontal velocity variation, results from Ghia et al. (1982).

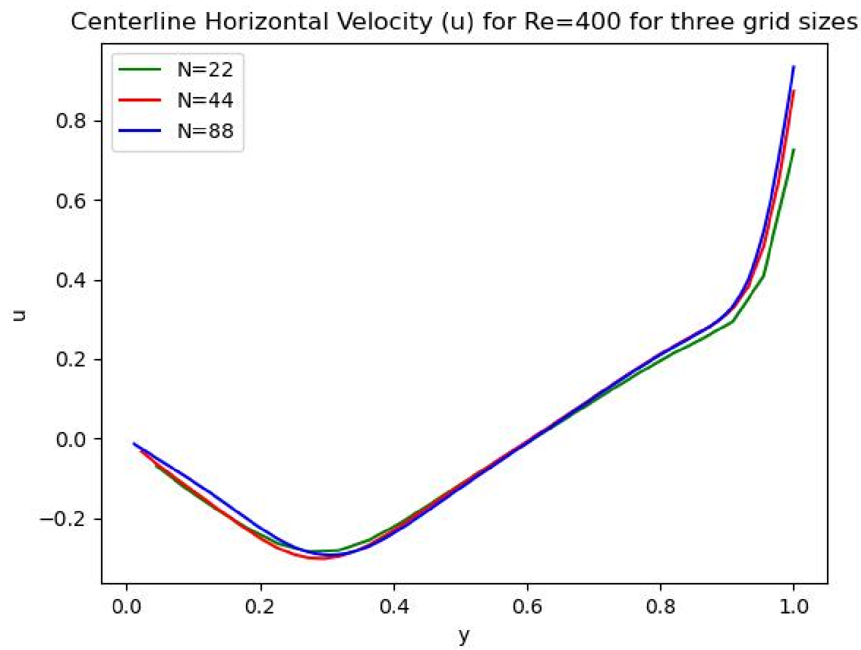

Figure 24: Centerline horizontal velocity for three grid sizes ($N = 22, 44, 88$) for $Re = 400$.

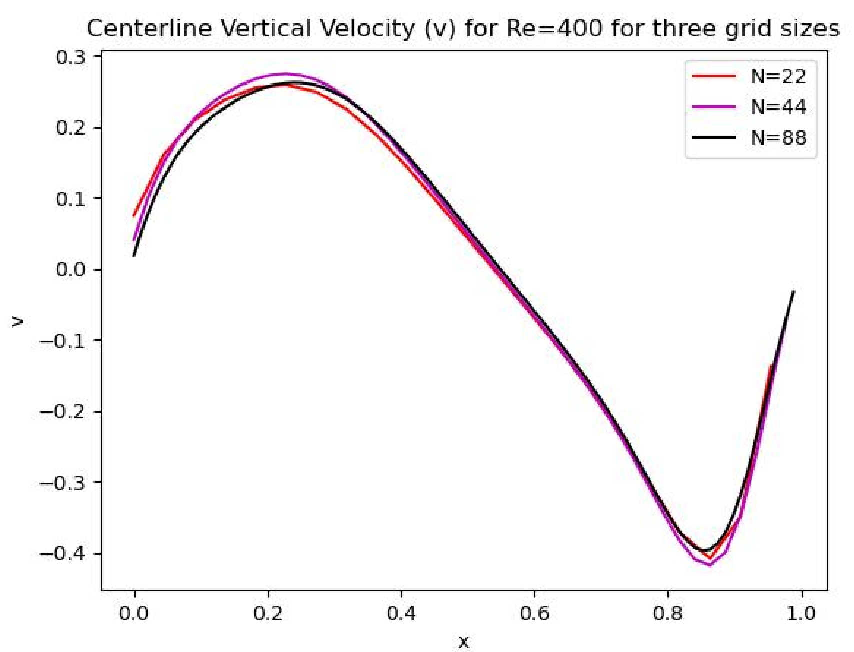

Figure 25: Centerline vertical velocity for three grid sizes ($N = 22, 44, 88$) for $Re = 400$.

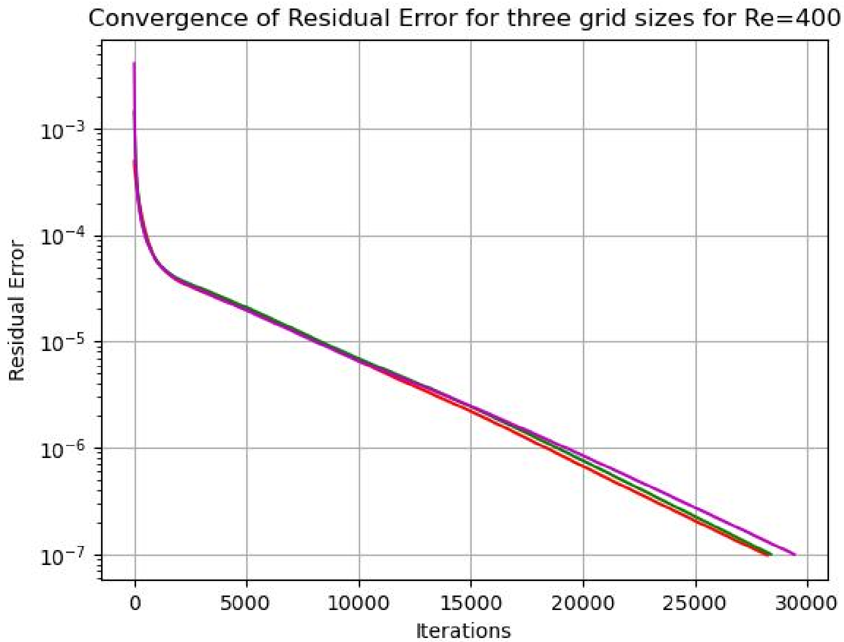

Figure 26: Plot of variation of residual with iterations for $N = 22$ (red), $N = 44$ (green), and $N = 88$ (magenta) for $Re = 100$.

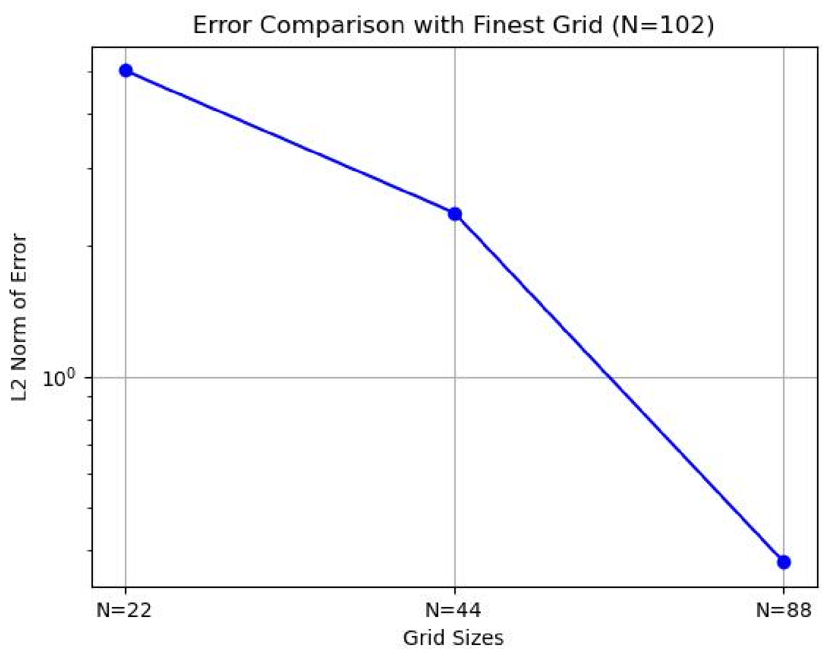

Figure 27: Plot of variation of residual with iterations for $N = 22$ (red), $N = 44$ (green), and $N = 88$ (magenta) for $Re = 400$.

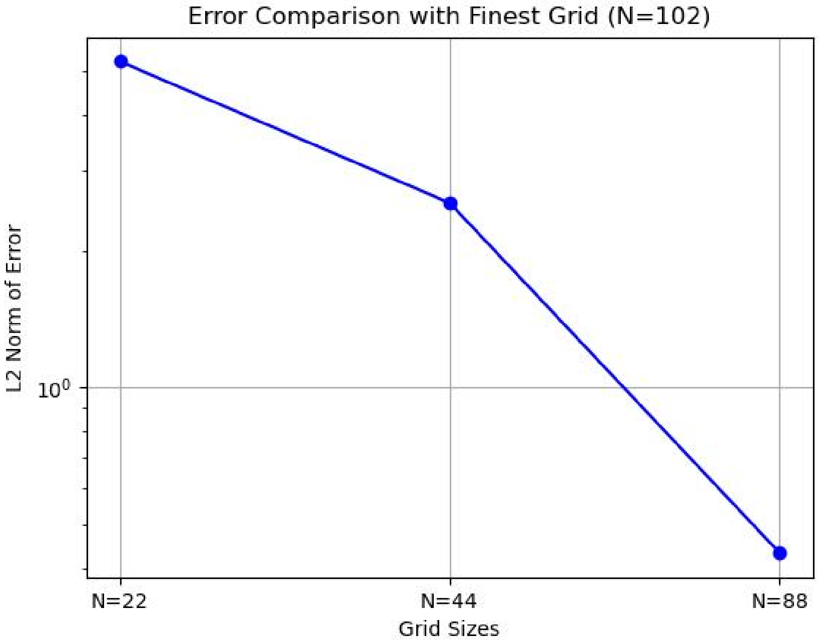

Figure 28: Error comparison with the finest grid ($N = 102$) for $Re = 100$.

both the momentum and pressure equations.

8 Comparison with the Artificial Compressibility Method

8.1 Application to time-dependent flows

The artificial compressibility method introduces a pseudo-time derivative into the continuity equation and is naturally suited to steady-state problems, where convergence in pseudo-time drives the velocity field toward incompressibility. Because the pseudo-time is not the physical time of the flow, the method is generally not as suitable for transient problems when the physical time evolution of pressure and velocity must be captured accurately.

By contrast, the projection method enforces incompressibility at every physical timestep by solving a pressure Poisson equation and correcting the intermediate velocity. This makes the projection method inherently well suited for time-dependent flows. The pressure field obtained through the Poisson equation is physically consistent with mass conservation at each timestep, so transient development can be represented more naturally.

8.2 Computational behavior

The artificial compressibility method can be attractive for steady problems because it avoids solving a pressure Poisson equation at every iteration. This can reduce the per-iteration computational cost, although the total number of iterations needed for pseudo-time convergence may be large. In

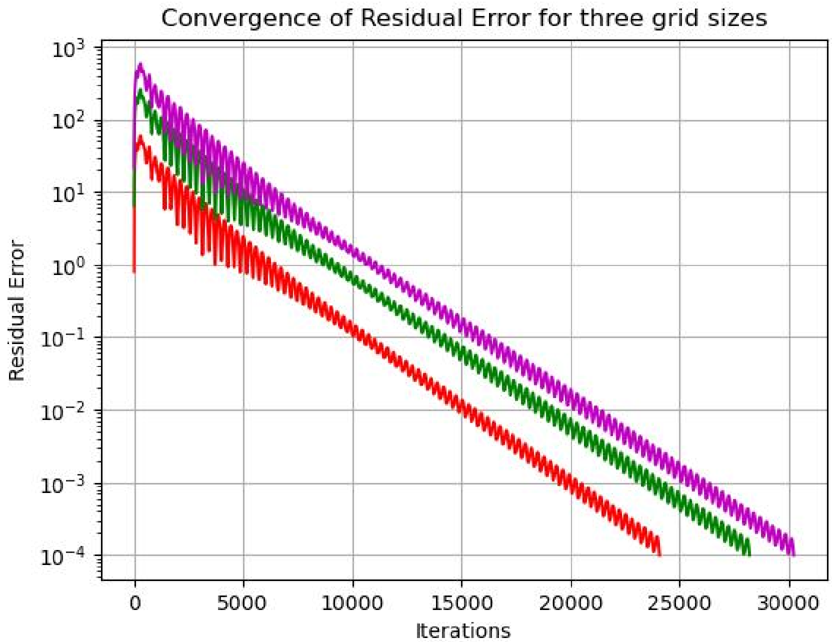

Figure 29: Convergence for $Re = 100$ for the artificial compressibility method.

addition, the method introduces an artificial compressibility parameter and an associated stability restriction that further limits the timestep.

The projection method is computationally more expensive per timestep because it requires the solution of a pressure Poisson equation. However, it produces a divergence-free velocity field at each timestep and generally offers better accuracy and robustness for transient incompressible flows. Its computational cost can be reduced through efficient Poisson solvers such as multigrid or conjugate-gradient-type approaches.

Overall, the projection method may require fewer physically meaningful timesteps to resolve transient flow behavior, although each timestep is more expensive. The artificial compressibility method, on the other hand, remains a conceptually simple and effective option for steady incompressible flows.

9 Conclusions

A staggered-grid projection-method solver was used to simulate the lid-driven cavity problem for Reynolds numbers $Re = 100$ and $Re = 400$. The method advances the momentum equations without pressure to obtain an intermediate velocity field, solves a pressure Poisson equation to enforce incompressibility, and then corrects the velocity to obtain a divergence-free solution.

The numerical results successfully captured the primary vortex, the growth of inertial effects with increasing Reynolds number, and the associated changes in centerline velocity profiles and corner recirculation behavior. Comparison with the benchmark data of Ghia et al. showed close agreement

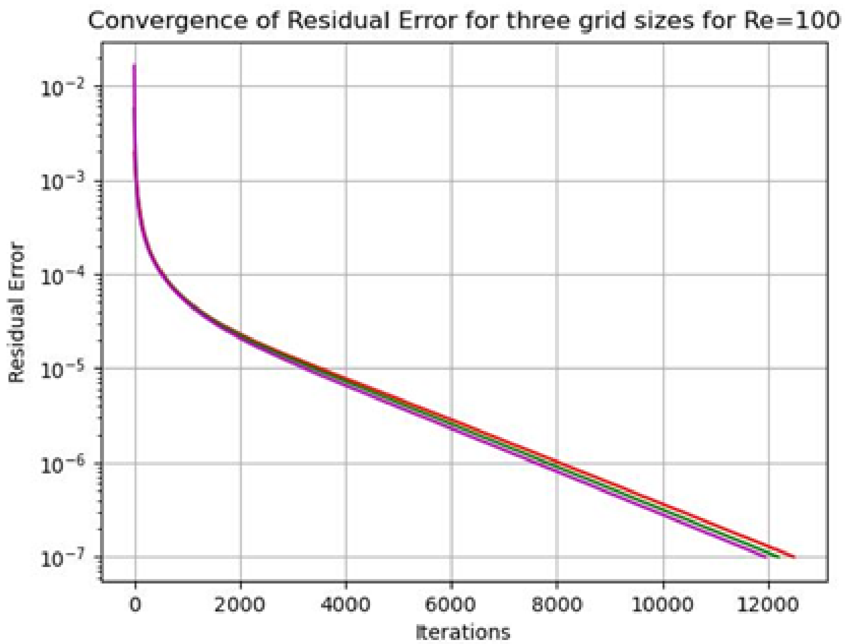

Figure 30: Convergence for $Re = 100$ for the projection method.

for both Reynolds numbers.

The grid-convergence and spatial-convergence studies demonstrated improved agreement with the benchmark solution as the mesh was refined, and the observed error trends were consistent with second-order spatial accuracy. The results also illustrate the key trade-off of the projection method: the additional computational effort associated with solving a pressure Poisson equation is balanced by stronger pressure–velocity coupling and better suitability for transient incompressible flows.

References

[1] A. J. Chorin, "Numerical solution of the Navier–Stokes equations," *Mathematics of Computation*, vol. 22, no. 104, pp. 745–762, 1968.

[2] U. Ghia, K. N. Ghia, and C. T. Shin, "High-Re solutions for incompressible flow using the Navier–Stokes equations and a multigrid method," *Journal of Computational Physics*, vol. 48, no. 3, pp. 387–411, 1982.

[3] A. J. Chorin, "Numerical solution of the Navier–Stokes equations," *Mathematics of Computation*, vol. 22, pp. 745–762, 1968.

[4] K. Goda, "A multistep technique with implicit difference schemes for calculating two- or three-dimensional cavity flows," *Journal of Computational Physics*, vol. 30, no. 1, pp. 76–95, 1979.

[5] J. Kim and P. Moin, "Application of a fractional-step method to incompressible Navier–Stokes equations," *Journal of Computational Physics*, vol. 59, pp. 308–323, 1985.

[6] J. van Kan, "A second-order accurate pressure-correction scheme for viscous incompressible flow," *SIAM Journal on Scientific and Statistical Computing*, vol. 7, no. 3, pp. 870–891, 1986.

[7] P. M. Gresho, "On the theory of semi-implicit projection methods for viscous incompressible flow and its implementation via a finite element method that also introduces a nearly consistent mass matrix. Part 1: Theory," *International Journal for Numerical Methods in Fluids*, vol. 11, pp. 587–620, 1990.

[8] P. M. Gresho and S. T. Chan, "On the theory of semi-implicit projection methods for viscous incompressible flow and its implementation via a finite element method that also introduces a nearly consistent mass matrix. Part 2: Implementation," *International Journal for Numerical Methods in Fluids*, vol. 11, pp. 621–659, 1990.